PNAS RESEARCH ARTICLE | BIOCHEMISTRY

Cryo-EM structure of the whole photosynthetic reaction center apparatus from the green sulfur bacterium *Chlorobaculum tepidum*

Hao Xie[a,1], Alexandros Lyratzakis[b], Radhika Khera[a], Myrto Koutantou[b], Sonja Welsch[c], Hartmut Michel[a,1], and Georgios Tsiotis[b,1]

Contributed by Hartmut Michel; received September 30, 2022; accepted December 27, 2022; reviewed by Alexey Amunts and C. N. Hunter

Light energy absorption and transfer are very important processes in photosynthesis. In green sulfur bacteria light is absorbed primarily by the chlorosomes and its energy is transferred via the Fenna–Matthews–Olson (FMO) proteins to a homodimeric reaction center (RC). Here, we report the cryogenic electron microscopic structure of the intact FMO-RC apparatus from *Chlorobaculum tepidum* at 2.5 Å resolution. The FMO-RC apparatus presents an asymmetric architecture and contains two FMO trimers that show different interaction patterns with the RC core. Furthermore, the two permanently bound transmembrane subunits PscC, which donate electrons to the special pair, interact only with the two large PscA subunits. This structure fills an important gap in our understanding of the transfer of energy from antenna to the electron transport chain of this RC and the transfer of electrons from reduced sulfur compounds to the special pair.

Cryo-EM | photosynthesis | reaction center | green sulfur bacterium | *Chlorobaculum tepidum*

Significance

Photosynthesis is the fundamental process that maintains life on Earth. The photosynthetic apparatus of green sulfur bacteria exhibits an unusual organization of their intermediate light-harvesting complexes. The energy absorbed by the chlorosome is transferred through Fenna–Matthews–Olson proteins to the reaction center (RC) to initiate charge separation and electron transfer. Here, we determined the cryo-EM structure of the whole photosynthetic RC apparatus from *Chlorobaculum tepidum* at 2.5 Å resolution. The structure of this photosynthetic RC complex, which exhibits features of both type I and II RCs, fills an important gap in our understanding of photosynthetic complex function and provides a basis for a more comprehensive examination of its energy and electron transfer functions through both experimental and theoretical approaches.

Photosynthesis is the most important energy conversion process on Earth. Light energy is captured by light-harvesting antenna complexes (LHCs) and subsequently converted to electrical and redox energy in the membrane-embedded photosynthetic reaction centers (RCs) (for review see ref. 1). During evolution, photosynthetic organisms developed different LHCs and RCs to adapt to various environments (2, 3). RCs are classified into two types based on the molecular identity of their terminal electron acceptors: type I RCs use a [4Fe–4S] cluster as the terminal electron acceptors, whereas type II RCs reduce quinones (4, 5). All anoxygenic phototrophic bacteria use either type I or type II RC for photosynthesis. Type I RCs are present in green sulfur bacteria (GSB, phylum *Chlorobiota*), *Heliobacteria* (phylum *Baccilota*), and phototrophic *Acidobacteria* (phylum *Acidobacteriota*), while purple photosynthetic bacteria (phylum *Pseudomonadota*), green filamentous non-sulfur bacteria (phylum *Chloroflexota*), and a phototrophic member of the *Gemmatimonadota* uses Type II RCs.

Unlike other photosynthetic organisms, members of the three phyla *Chlorobiota, Acidobacteriota*, and *Chloroflexota* use chlorosomes for light harvesting, in which the major light-harvesting pigments are organized in self-assembled supramolecular aggregates rather than on protein scaffolds (6). The envelope of a chlorosome contains a baseplate that is oriented toward the cytoplasmic membrane as a two-dimensional paracrystalline array (7). The baseplate is formed by multiple copies of the CsmA protein, each binding one bacteriochlorophyll *a* (BChl *a*) pigment molecule. Light energy captured by the bacteriochlorophylls (BChls) in chlorosomes is trapped by BChl *a* in the baseplate and transferred subsequently towards the RC. In GSB and phototrophic *Acidobacteria*, the baseplate is attached to an intermediate light-harvesting complex, the Fenna–Matthews–Olson (FMO) protein. FMO is a water-soluble BChl *a*-binding protein that is peripherally located outside the cytoplasmic membrane. On the one hand, FMO serves as an interconnecting node, mediating the transfer of excitation energy from the chlorosome to the RC. On the other hand, FMO forms a space between the chlorosome and the cytoplasmic membrane, allowing the diffusion of downstream redox mediators such as ferredoxin (6). Recently, as reported by Tsuji et al. (8), a member of the *Chloroflexota* phylum was also found to employ type I RC and FMO proteins for anoxygenic phototrophy, although all previously characterized *Chloroflexota* members use a type II RC to perform light energy conversion and lack FMO.

Chlorobaculum tepidum (*C. tepidum*) is a thermophilic anaerobic GSB that utilizes reduced sulfur compounds as electron donors to the photosynthetic electron transport chain during anoxygenic photosynthesis (9). The RC of this bacterium (GsbRC, type I) consists of six subunits: two 82-kDa core subunits (PscA), one 24-kDa iron/sulfur protein (PscB), two 23-kDa cytochrome c_z proteins (PscC) and one 17-kDa protein (PscD). Analogous to the heterodimer PsaA/PsaB of photosystem I (PSI) and to the PshA

Author contributions: H.X. and G.T. designed research; H.X., A.L., and G.T. performed research; S.W. contributed new reagents/analytic tools; H.X., A.L., R.K., H.M., and G.T. analyzed data; M.K. assisted for protein purification; and H.X. and G.T. wrote the paper.

Reviewers: A.A., Stockholms universitet Institutionen for biokemi och biofysik; and C.N.H., University of Sheffield.

The authors declare no competing interest.

Copyright © 2023 the Author(s). Published by PNAS. This article is distributed under Creative Commons Attribution-NonCommercial-NoDerivatives License 4.0 (CC BY-NC-ND).

[1]To whom correspondence may be addressed. Email: Hao.Xie@biophys.mpg.de, Hartmut.Michel@biophys.mpg.de, or tsiotis@uoc.gr.

This article contains supporting information online at https://www.pnas.org/lookup/suppl/doi:10.1073/pnas.2216734120/-/DCSupplemental.

Published January 24, 2023.

Downloaded from https://www.pnas.org by MPDL BIOPHYSIK on February 16, 2023 from IP address 194.95.30.10.

homodimer of type I RC from *Heliobacteria* (HbRC), the PscA homodimer of GsbRC carries the primary electron donor P_{840} (a special pair of two BChl *a* molecules), the primary electron acceptor A_{CC}, the secondary electron acceptor A_0 and an interpolypeptide [4Fe–4S] cluster (F_X) as the intermediate electron acceptor (10). The special pair accepts energy from chlorosomes transferred via the FMO and electrons from reduced sulfur compounds via the PscC subunit (11, 12). The PscB subunit, which resembles the PsaC subunit of PSI, contains the two [4Fe–4S] centers F_A and F_B, with F_B being the terminal electron acceptor, donating electrons to ferredoxin.

Previous studies revealed that GsbRC associates with FMO, forming an FMO-GsbRC complex (13, 14). Scanning transmission electron microscopy analysis of Triton X-100-solubilized and negatively stained GsbRC showed one firmly bound FMO trimer on the cytoplasmic side of the GsbRC (14). The presence of an FMO-GsbRC complex formed by one GsbRC and two FMO trimers was also suggested by further studies (10, 13). Furthermore, a photosynthetic supercomplex consisting of two GsbRCs and four FMO trimers was proposed to represent the functional form in the native membrane (15). Recently, the cryogenic electron microscopic (cryo-EM) structure of a Triton X-100-solubilized FMO-GsbRC subcomplex containing seven subunits (PscA-1, PscA-2, PscB, PscD, FMO-1 to 3) has been reported (16). This structure gives insights into the protein organization, chromophore location and association of one FMO trimer with the core subunits of the RC complex (16). However, to date, the structural basis for the energy transfer from the complete peripheral antennas as well as from PscC to the P_{840} has remained elusive.

Results and Discussions

Structure of the Whole FMO-GsbRC Complex. The whole FMO-GsbRC complex was purified by a modification of previously reported methods (13). Modifications include the detergent exchange from n-dodecyl-β-D-maltoside (DDM) to lauryl maltose neopentyl glycol (LMNG) and a combination of gradient-based detergent removal (GraDeR) (17) and gradient fixation (GraFix) (18) approaches (*SI Appendix*, Fig. S1*A*). Four colored bands (RC1 to RC4) were observed after the last density-gradient centrifugation step (*SI Appendix*, Fig. S1*A*). They were recovered and further analyzed by blue native polyacrylamide gel electrophoresis (BN-PAGE), mass spectrometry, negative-stain EM, and cryo-EM. Our results revealed that the uppermost band RC1 represents free FMO trimer, while RC2 to RC4 were heterogeneous with respect to the subunit composition. RC2 mainly contains the membrane core of the GsbRC, while RC3 mainly represents the FMO-GsbRC subcomplex (one RC with one FMO trimer). The lowest band RC4 used for cryo-EM analysis in this work shows one major band of about 600 kDa on BN-PAGE gel (*SI Appendix*, Fig. S1*C*) and contains mainly the whole RC with two FMO trimers as also confirmed by negative-stain EM (*SI Appendix*, Fig. S1 *D* and *E*). The applied isolation protocol allowed the purification of the whole photosynthetic RC complex with 12 subunits in contrast to the reported subcomplex structure, in which structural information for five subunits, namely the two PscC and three FMO subunits is missing (16).

We determined the structure of the whole FMO-GsbRC complex at 2.5 Å resolution by cryo-EM (Fig. 1 and *SI Appendix*, Figs. S2–S4 and Table S1 and Movie S1). Its overall dimensions are approximately 180 × 110 × 125 Å (Fig. 1 *A* and *C*), and it is made up of 12 protein subunits (~490 kDa): four subunits (PscA-1, PscA-2, PscC-1, and PscC-2) form the membrane core, two peripheral subunits (PscB and PscD) and six FMO proteins (FMO-1 to 6) are arranged as two FMO trimers (Fig. 1). In addition, our model accommodates a total of 91 cofactors: 78 chlorophylls, 6 lipids, 2 carotenoids, 3 [4Fe–4S] clusters and 2 calcium ions (Movie S2). Previous studies identified three major carotenoids in GsbRC from *C. tepidum* strain TLS: chlorobactene, OH-γ-carotene glucoside ester, and OH-chlorobactene glucoside laurate (19, 20). In the recently reported FMO-GsbRC subcomplex structure, two carotenoids were assigned in each PscA subunit. An OH-chlorobactene glucoside laurate (F39) is closely associated with both cytoplasmic and periplasmic BChl layers, while a chlorobactene (F26) is present in the cytoplasmic BChl layer (16). In our EM map, two extra densities were also observed at the same positions (*SI Appendix*, Fig. S5). One was assigned as F39, which is in accordance with the previously published result. However, the second extra density cannot be unequivocally interpreted, because the fitting of a chlorobactene (F26) resulted in a structural clash between its aromatic head and the transmembrane helix 3 (TMH3) of PscC subunit (*SI Appendix*, Fig. S5*D*), which was mainly attributed to the relatively low local resolution. Nevertheless, we consider that a large fraction of the second extra density must be due to the presence of F26, because the previous study showed that chlorobactene is one of the major carotenoids present in the isolated GsbRC (20). For each PscA subunit in our structure, two lipids were assigned as a phosphatidylglycerol (PG, 16:0/16:0) and a monogalactosyldiacylglycerol (MGDG, 16:0/16:1), which are adjacent to the above-mentioned F39 (*SI Appendix*, Fig. S5*B*). These results are in good agreement with the previously published results (16, 21, 22). In addition, we modeled a second PG (16:0/16:0) into an extra density close to the A_1 site (*SI Appendix*, Fig. S5*C*). A similar density was also observed in the recently reported FMO-GsbRC subcomplex structure, but remained unmodeled (16). Fitting of a PG into this density has been also suggested by previous studies (5).

The membrane core of GsbRC consists of two PscA and two PscC subunits, assembled as a dimer of the heterodimer (Fig. 1 *A* and *D*) (23). The structural arrangement of 22 transmembrane helices (TMHs) in the two PscA subunits is similar to that of the PshA homodimer of HbRC (24) and nearly identical to that of the FMO-GsbRC subcomplex (16) (*SI Appendix*, Fig. S6). The PscA subunit can be divided into an antenna domain comprising the first six TMHs and an electron transfer (ET) domain comprising the last five TMHs. The three TMHs of each PscC subunit are symmetrically located around the PscA homodimer. The spatial arrangement of the 28 TMHs exhibits C_2 symmetry with the rotational axis of symmetry perpendicular to the membrane plane (Fig. 1*A*). Unlike all other RCs, whose electron donors to the special pair are soluble, membrane-associated or membrane-tethered proteins, only GsbRC employs a transmembrane protein subunit to deliver electrons (5). In our structure, only the N-terminal membrane part of both PscC subunits (residues 5 to 125) could be modeled (*SI Appendix*, Fig. S7). Its periplasmic C-terminal domain, which contains the heme *c* (25), was not resolved in the EM density map, likely due to high flexibility. This functional domain has been proposed to be highly mobile and to fluctuate between the cytochrome bc_1 complex and the P_{840} during the photosynthetic ET (26). The three TMHs of PscC are connected in an up–down–up topology and lie roughly in the same plane that is in contact with the peripheral surfaces of PscA (Fig. 2*B*1). In the case of PscC-1, its first two TMHs interact with the ET domain of PscA-1 mainly through the connecting loop, while the TMH3 interacts solely with the antenna domain of the PscA-2 (Figs. 1D and 2*B*1). Furthermore, TMH2 and 3 partially cover the major groove of

Downloaded from https://www.pnas.org by MPDL BIOPHYSIK on February 16, 2023 from IP address 194.95.30.10.

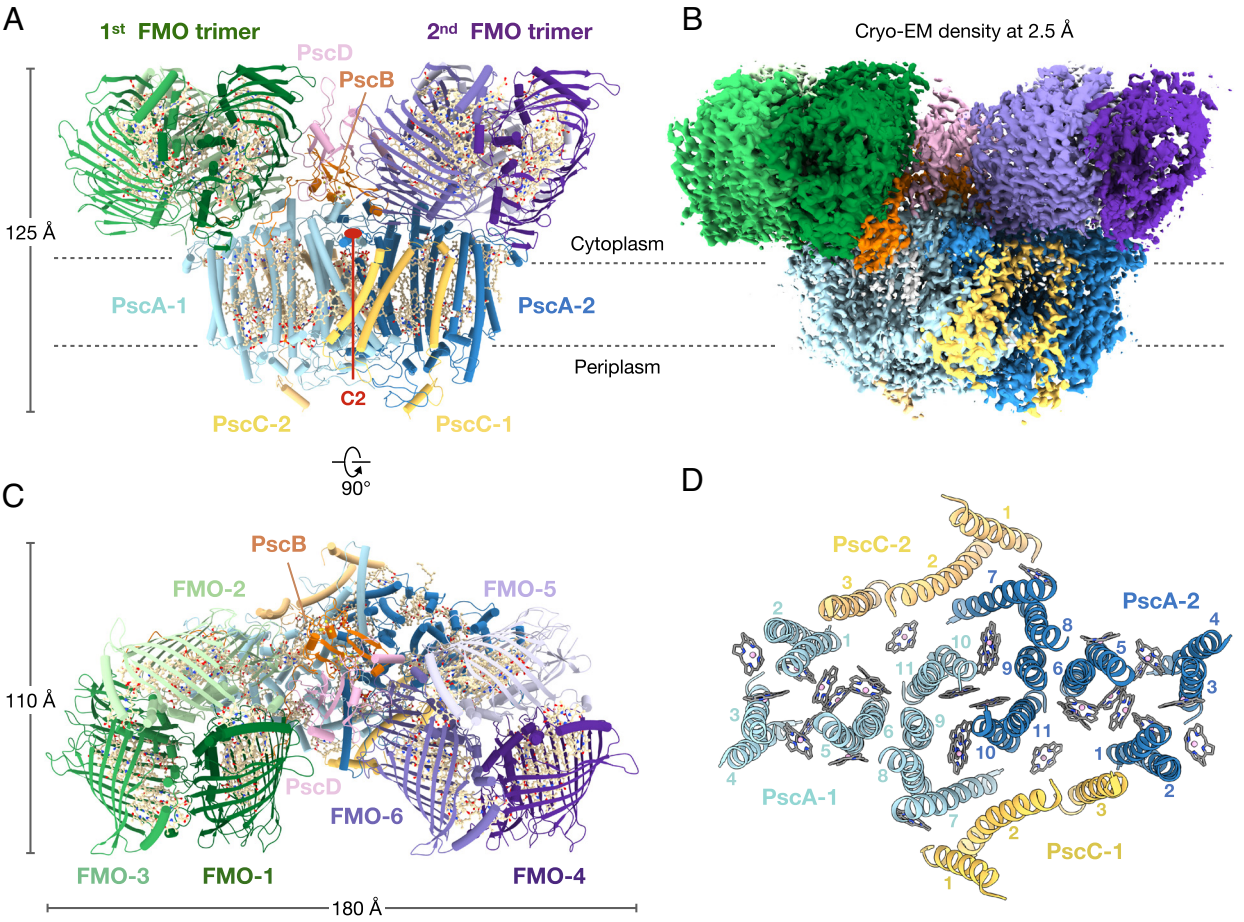

Fig. 1. Cryo-EM structure of whole FMO-GsbRC complex. (*A* and *C*) Overall structure of the whole FMO-GsbRC complex from *C. tepidum* with views from the side (*A*) and top (*C*). Individual subunits are shown in cartoon representation and colored differently. Cofactors (chlorophylls, lipids, carotenoids and Fe-S clusters) are shown as ball-and-stick structures in wheat. (*B*) Surface representation of the cryo-EM density map (2.5 Å) of the whole FMO-GsbRC colored as in *A*. (*D*) Arrangement of the TMHs and the pigments of the whole FMO-GsbRC. TMHs of the two PscA subunits are colored in blue and labeled 1 to 11, from N- to C-terminus. TMHs of the two PscC subunits are colored in yellow and labeled 1 to 3, from N- to C-terminus. Chlorophylls are shown as sticks in grey, with the magnesium ions in pink.

PscA-2 on one side, which is formed between the antenna domain and the ET domain of PscA-2 (Fig. 2*B*2). In addition, PscC-1 is in close contact with the chromophores involved in energy transfer (BChl-815) and ET (A_{CC} and A_0). These helical arrangements may help to provide a more stable environment for energy transfer between the antenna and ET domains by preventing a direct exposure of the nearby chromophores to the lipid bilayer. Furthermore, PscC possesses a periplasmic loop, stretching from residues 101 to 115. This loop is sandwiched between two solvent-exposed loop regions from PscA-2 and followed by a short helix (Fig. 2*B*3). Several ionic interactions are observed in this region, which provide structural rigidity to this segment. Therefore, this region may serve as a potential pivot point allowing the soluble cytochrome *c* domain to shuttle between P_{840} and the electron donor of PscC. In addition, TMH1 of PscC is located in approximately the same position as the PsaF subunit in PSI (27) (*SI Appendix*, Fig. S7*C*), which is essential for the ET from the soluble electron carrier plastocyanin or cytochrome c_6 to the P_{700} of PSI (28).

The C_2 symmetry of the membrane core cannot be applied to the whole complex mainly due to the presence of the PscB and PscD subunits, which are located on the cytoplasmic side of the complex. For PscB, our model includes two parts: residues 139 to 228 and an N-terminal region (residues 60 to 80, hereafter termed as N-arm) that is missing in the previously reported subcomplex structure (16). This N-arm is located between two intrinsically disordered regions (*SI Appendix*, Fig. S8) and solely interacts with the first FMO trimer (Fig. 2*C*1). Similar to the PsaC subunit of PSI, the PscB of GsbRC contains two [4Fe–4S] centers F_A and F_B that are essential for the photochemical activity by donating electrons to ferredoxin. For PscD, we modeled residues 18 to 101 and 109 to 143, comprising ~83% of its total amino acid residues (*SI Appendix*, Fig. S9). In the C-terminal region of PscD, remarkable differences were noticed between our model and the recently reported one (*SI Appendix*, Fig. S9*C*), especially for residues 87 to 117. Furthermore, residues 117 to 143 were missing in the previously published structure (*SI Appendix*, Fig. S9*C*). PscB and PscD interact with each other, as well as with the membrane core and FMO. They may serve as the electron exit site and are essential for promoting the FMO-RC interaction, complex integration and ferredoxin docking.

The two FMO trimers are structurally nearly identical, as indicated by the low rmsd of 0.12 Å for 1,072 pairs of Cα atoms. Both FMO trimers are connected to the membrane core of GsbRC primarily via interactions with PscB and PscD, and each FMO trimer interacts only with the distal end of its adjacent PscA subunit (Fig. 2 *A* and *D*). Contrary to the previous assumption that both FMO trimers are symmetrically arranged around the C_2 axis of the membrane core (16), they are asymmetrically positioned on the cytoplasmic side of PscA (Fig. 3). As compared to the first FMO trimer, the second is shifted toward the central axis of the membrane core (Fig. 3*A*). This

Downloaded from https://www.pnas.org by MPDL BIOPHYSIK on February 16, 2023 from IP address 194.95.30.10.

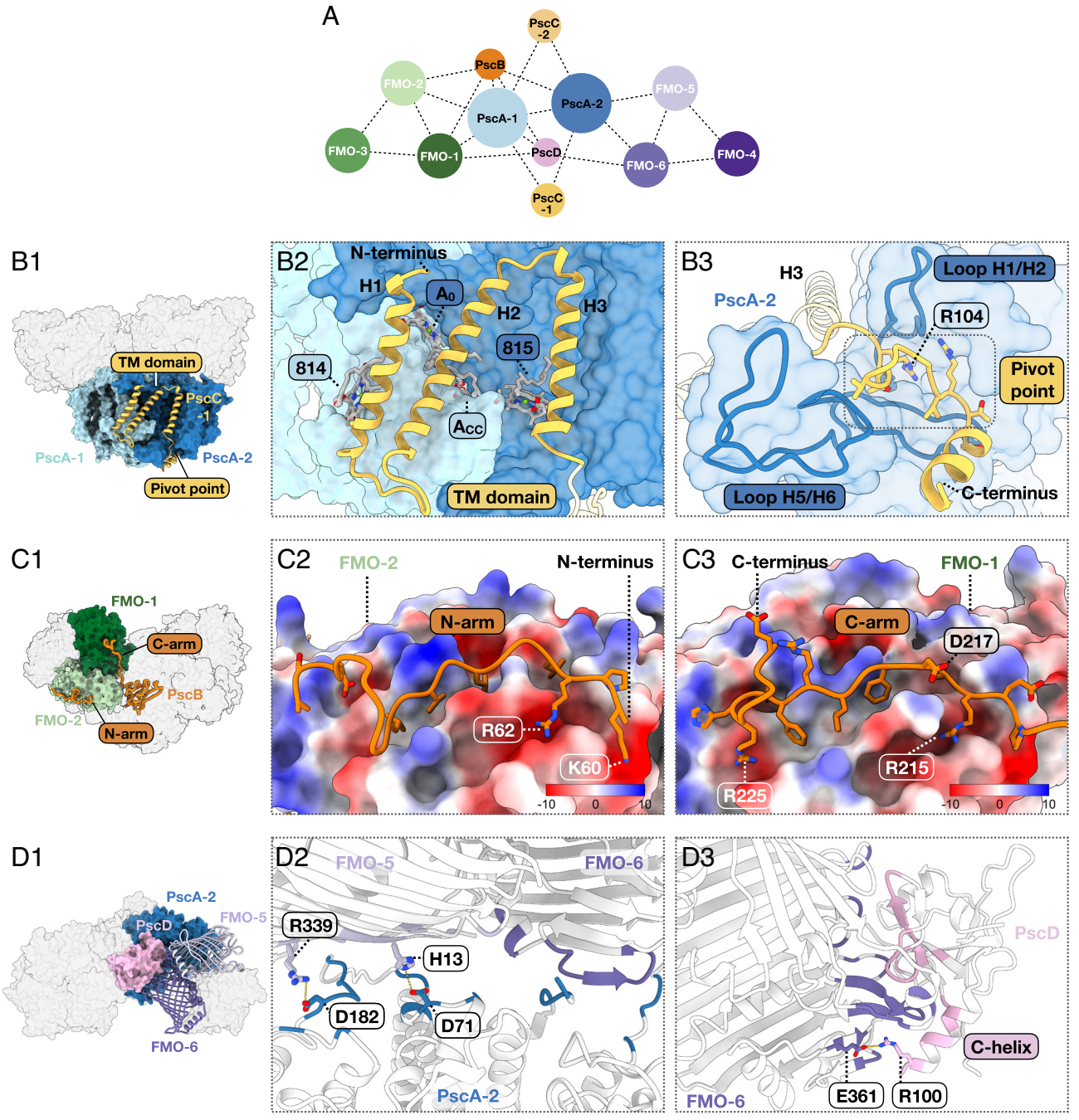

Fig. 2. Schematic representation of the intersubunit interactions. (*A*) The intrinsic interactions between subunits of the FMO-GsbRC complex shown as dotted lines. Node sizes are proportional to the solvent accessible surface area of each subunit. Buried surface areas between subunits are listed in *SI Appendix*, Table S2. (*B1*) Interaction between PscC (yellow) and PscA (blue). (*B2*) Interaction of the three TMHs of PscC with the PscA and the energy and electron transport chromophores. (*B3*) Interaction of the periplasmic loop of PscC with PscA. (*C1*) Interaction between PscB (orange) and the first FMO trimer (green). (*C2*) Interaction between the N-arm of PscB and FMO-2. (*C3*) Interaction between the C-arm of PscB and FMO-1. Interacting residues from PscB, which form salt bridges with various residues of FMO, are labeled. The electrostatic surface potential of FMO proteins is shown from −10 kT/e (red) to +10 kT/e (blue). (*D1*) Interaction between PscD (pink), the second FMO trimer (purple) and PscA-2 (blue). (*D2*) Interaction between the second FMO trimer and PscA-2. (*D3*) Interaction between the second FMO trimer and PscD. All interfacing residues are colored. Residues forming salt bridges are labeled.

asymmetrical arrangement is probably caused by the different interaction patterns of FMO trimers toward GsbRC. In particular, the C-and N-terminal arms of PscB, acting as a molecular clamp, are entwined around the first FMO trimer by interactions with FMO-1 and FMO-2, respectively (Fig. 2*C*). Several residues at this inter-subunit interface are involved in hydrophobic and ionic interactions, indicating a relatively strong association (Fig. 2*C*). In addition, PscD interconnects with FMO-1 and FMO-6 from the first and second FMO trimer, respectively (Fig. 2*A*). This linkage correlates well with the results observed from time-resolved fluorescence measurements, revealing an essential role of PscD in efficient energy transfer from chlorosomes to the RC via FMO proteins (29). Furthermore, previous studies showed that the dissociation of PscB/PscD from the whole complex is intrinsically linked to loss of FMO trimers as well (23, 30). In contrast to the first FMO trimer, the second FMO trimer employs only FMO-6 for the interaction with PscD, and shows only weak connections

Downloaded from https://www.pnas.org by MPDL BIOPHYSIK on February 16, 2023 from IP address 194.95.30.10.

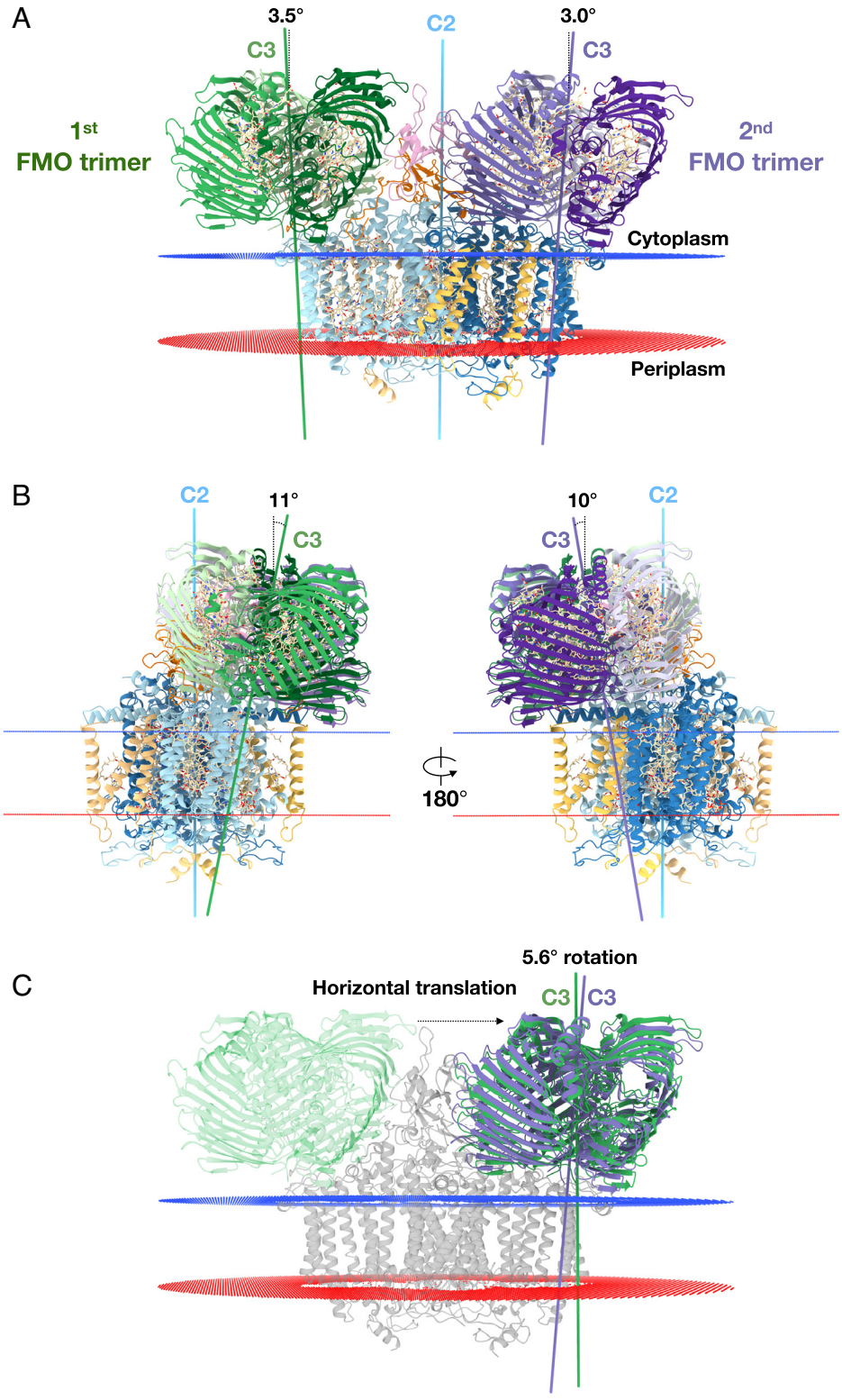

Fig. 3. Asymmetrical arrangement of the two FMO trimers. (*A*) The two PscA subunits are related by a twofold symmetry axis (C_2, blue line) perpendicular to the membrane plane. The threefold symmetry (C_3) axes of the first and second FMO trimer are indicated as green and purple lines, respectively. From this side view, the C3 axes of the first and second FMO trimer form a 3.5° and 3.0° angle with the membrane normal. (*B*) Similar to *A* but rotated ± 90° around the membrane normal. Two side views are related by a 180° rotation. (*C*) Comparison of both FMO trimers. The first FMO trimer is horizontally moved to align with the second FMO trimer. The two C3 axes are related by a 5.6° rotation. The membrane boundary was defined by the PPM server (31).

with the adjacent PscA-2 (Fig. 2 *A* and *D*). Taken together, our results suggest that, as compared to the first FMO trimer, the second FMO may be incorporated into the GsbRC complex with high flexibility that provides structural plasticity for interaction both with the chlorosome and RC. Future studies will be needed to comprehensively investigate the dynamic interaction between FMO and RC, in particular in the presence of chlorosome baseplate.

Downloaded from https://www.pnas.org by MPDL BIOPHYSIK on February 16, 2023 from IP address 194.95.30.10.

Possible Energy Transfer Pathways from the Chlorosomes to the Special Pair P_{840}. The arrangement of the pigments in FMO-GsbRC complex is similar to recent findings in the FMO-GsbRC subcomplex (Fig. 4) (16). Each FMO trimer consists of three identical FMO monomers and each of the three monomers contains eight BChl *a* molecules (BChl-1 to 8) (32, 33). Previous studies suggested that the FMO trimer lies flat on the cytoplasmic membrane with its C_3 symmetry axis perpendicular to the membrane plane (34). This orientation enables all three BChl-8 from three FMO monomers to attach to the baseplate and to contribute equally to the energy acquisition and allocation. On the contrary, our structure shows that the C_3 symmetry axes of both FMO trimers are tilted ~10° to the membrane normal and are not parallel to each other (Fig. 3). As a consequence of the tilt, in each FMO trimer only two FMO monomers are in close contact with the chlorosome, while the third one is inclined to the cytoplasmic membrane. Therefore, only two BChl-8 exposed at the uppermost surface, may efficiently receive energy from the chlorosome (Fig. 4). Previous studies showed that BChl-8 is strongly excitonically coupled to BChl-1 of the nearest-neighboring FMO monomer, revealing an inter-monomer energy transfer (35). Consequently, the excited BChl-8 will transfer its energy to BChl-1 of the adjacent FMO and finally to BChl-3 (35–37).

At the interface between FMO and PscA, differences can be found with regard to the arrangement of pigments involved in energy transfer (Fig. 4*A*). For the energy transfer from the first FMO trimer to PscA-1, the shortest edge-to-edge distance between two BChls is 21.5 Å from BChl-3 of FMO-2 to BChl-808 (Fig. 4*B*). Similar distances are also observed between BChl-3 of FMO-1 and BChl-810. In contrast, BChl-3 of FMO-3 is positioned 32.6 Å distant from the nearest BChl in the core. The close distances are consistent with the consensus that BChl-3 is the lowest energy site and therefore serves as a bridge conducting excitation energy from the FMO to the membrane core (38). In the case of the second FMO trimer, the shortest BChl-to-BChl distance is 22.5 Å from BChl-3 in FMO-5 to BChl-808 of PscA-2, while the other two FMO monomers, FMO-4 and FMO-6, are located further away (Fig. 4*C*). In addition, PscA-2 may also use BChl-807 to receive transferred energy from BChl-3 of FMO-5, because the two BChl molecules have a distance of 23.4 Å, which is slightly longer than that observed between BChl-3 of FMO-5 and BChl-808. Despite these differences, the observed distances suggest, on one hand, that only one or two proximal monomers are employed for the direct energetic coupling between the FMO trimer and the membrane core. On the other hand, the energy received by the distal FMO monomer(s) may initially proceed through an adjacent FMO monomer rather than directly to PscA, indicating an asymmetrical energy coupling. The latter is concordant with previous findings showing that most of the FMO proteins (about 66%), regardless of the fact that they were physically attached to the RC, cannot transfer excitation energy (39). Given that our structure was solved in the detergent-solubilized state and in the absence of the chlorosome baseplate, it is conceivable that FMO may adopt other orientations in vivo with respect to the chlorosome. Nevertheless, the location of three FMO monomers within the same trimer relatively to the membrane core will not be substantially changed. The asymmetrical energy coupling, together with the relatively long distances between BChls of FMO and the closest BChls in PscA, may provide an explanation for the low energy transfer efficiency of 40 to 75% (39, 40), which is far lower than near the 100% for the energy transfer between light-harvesting complex I (LHCI) and PSI RC (41).

As can be seen from the structure of the FMO-GsbRC complex, each FMO trimer is only constrained by one neighboring PscA, suggesting the presence of two independent energy transfer pathways (Fig. 4). The energy received by one PscA must be transferred within the same subunit through a network of pigments to the special pair P_{840}. As observed in the previously reported subcomplex structure (16), the two PscA subunits bind only 24 antenna BChls, far fewer than the number found in HbRC (54 BChls) (24) and in PSI [90 (B)Chls] (27) but similar to that in PSII [31 (B)Chls) (42). The 24 antenna BChls are separated into two layers (cytoplasmic and periplasmic, respectively) with the shortest edge-to-edge distance of 7.2 Å from BChl-804 to BChl-812 (*SI Appendix*, Fig. S10). As previously reported (16), each PscA binds one glycosylated chlorobactene (F39), which is in close association with both BChl layers and may function as a direct quencher of excess excitation energy. The energy, which enters the cytoplasmic BChls, is transferred to the periplasmic BChl layer and finally reaches P_{840} through BChl-811 and BChl-815, because these two BChls are located closest to P_{840} with Mg-to-Mg distances of 20.4 and 18.9 Å, respectively (Fig. 4*E*).

Possible ET Pathways in GsbRC. In GsbRC, electronic excitation of P_{840} leads to the formation of the charge-separated state and subsequent ET from P_{840} to A_{CC}. The photo-oxidized P_{840}^{+} is re-reduced by subunit PscC (cyt. c_z), which can receive electrons derived from sulfide or thiosulfate oxidation (43). To investigate the ET and interaction modes between GsbRC and cyt. c_z, we have performed a protein–protein docking analysis using the crystal structure of the C-terminal cytochrome domain of PscC (25), since this region was not visible in our structure (Fig. 1 and *SI Appendix*, Fig. S7). Our results show that, similar to the cyanobacterial PSI (44) and the purple bacterial RC (PbRC, type II) (45), GsbRC has only one binding site for cyt. c_z (Fig. 5*A*). According to our binding mode, the heme *c* is located in the crevice of cyt. c_z with its two propionate groups exposed to the solvent and towards the binding site formed by two parallel tryptophan residues from both PscA subunits ($W601^{PscA}$) (Fig. 5*B* and *SI Appendix*, Fig. S11). The exposed edge of the heme is surrounded by two positively charged residues ($K168^{PscC}$ and $R181^{PscC}$) that interact with the negative charges of PscA. The two tryptophan residues are also conserved at the docking interface between cyanobacterial PSI and cyt. c_6, although they originate from two different subunits, PsaA and PsaB (44). The shortest center-to-center distance between the heme group and the primary donor P is 21.9 Å for GsbRC-cyt. c_z, which is very similar to that observed for PSI-cyt. c_6 (21.3 Å) (44) and for PbRC-cyt. c_2 (21.1 Å) (45) (*SI Appendix*, Fig. S11). These results indicate that, despite the overall low sequence identity, different RCs have diverged only slightly from one another with respect to the relative positioning between the electron carriers and the special pair. In addition, the presence of two independent energy transfer pathways but only one binding site for the ET opens up the discussion of how the reduced cytochromes from both PscC communicate in the supply of electrons to the special pair.

The primary charge separation event is followed by ET from F_X to the terminal electron acceptors, F_A and F_B, and further to ferredoxin. In PSI, the ferredoxin binding site comprises several basic residues in the PsaA and PsaC subunits (46). In our structure, we observed that several positively charged residues ($K149^{PscB}$, $K153^{PscB}$, $K45^{PscA}$, $R47^{PscA}$, and $R48^{PscA}$) are also clustered in the proximity of the F_B site (Fig. 5*C*), indicating a similarity of the residue composition of the ferredoxin binding site in GsbRC and PSI. These structural data also correlate with the observation that

Downloaded from https://www.pnas.org by MPDL BIOPHYSIK on February 16, 2023 from IP address 194.95.30.10.

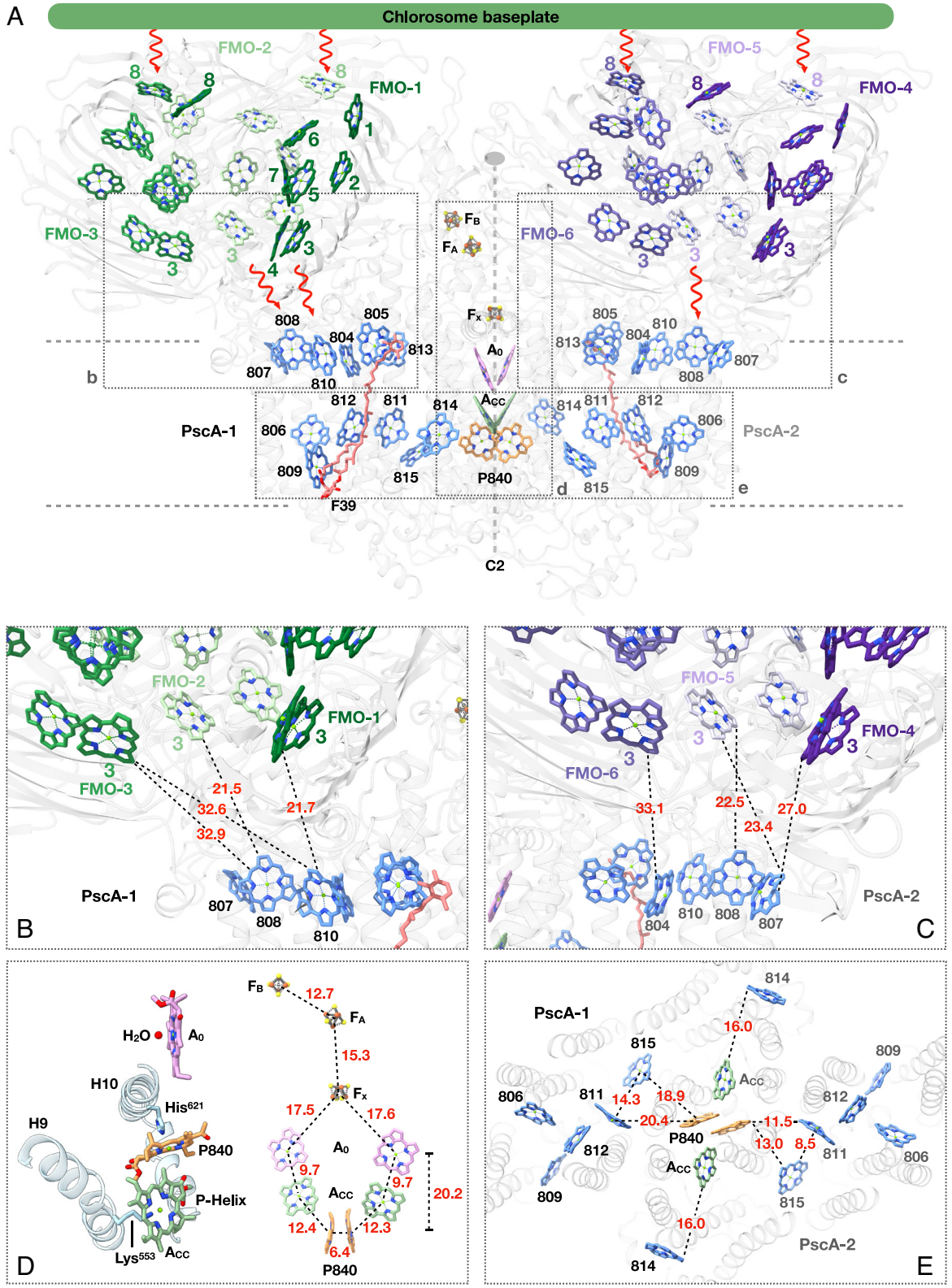

Fig. 4. Possible energy transfer pathways in the FMO-GsbRC complex. (*A*) Putative energy transfer pathways from chlorosome via the FMO trimers and eventually to GsbRC. Areas in the dashed boxes are enlarged in subsequent panels. (*B*) Intermolecular interface between the first FMO trimer and PscA-1. (*C*) Intermolecular interface between the second FMO trimer and PscA-2. (*D*) Cofactor arrangement along the electron transport chain in GsbRC. The left panel shows the coordinating environment for the three chlorophyll cofactors. The coordinating residues are indicated, and the water molecule serving as an axial ligand to A_0 is shown as a red sphere. (*E*) Possible energy transfer from BChls to the special pair P_{840}. Antenna BChls (811, 814 and 815) are located between the bulk BChls of RC and electron transport chain in the periplasmic BChl layer. All Chl molecules are colored according to the scheme used in Fig. 1. ET cofactors are colored differently for better viewing: P_{840} (orange), A_{CC} (green), and A_0 (purple). The phytyl tails of BChls and Chls were truncated for ease of viewing. Center-to-center or edge-to-edge distances are indicated as dashed lines and in angstrom (red numbers).

Downloaded from https://www.pnas.org by MPDL BIOPHYSIK on February 16, 2023 from IP address 194.95.30.10.

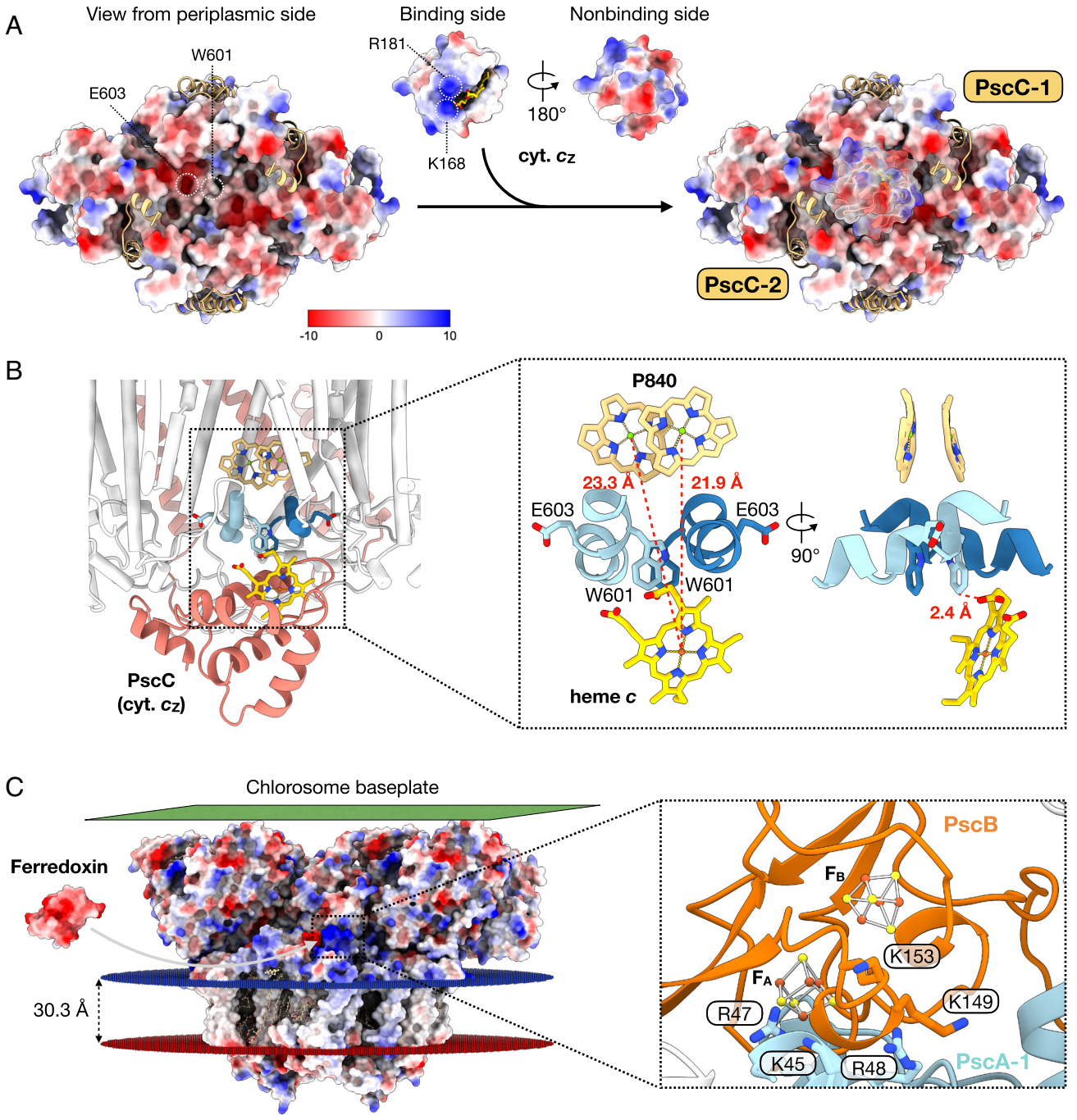

Fig. 5. Possible electron transport in the FMO-GsbRC complex. (*A*) Electrostatic surface representation of the FMO-GsbRC complex showing the potential docking site for cyt. c_z. The *Left* panel shows the periplasmic side of PscA without cyt. c_z, the *Middle* panel shows the cyt. c_z alone and the *Right* panel shows the complex with the binding of cyt. c_z. The PscC subunits are shown in cartoon representation. The protein surface is colored according to its electrostatic potential from red (−10 kT) to blue (+10 kT). Residues, which may be involved in a specific binding of cyt. c_z, are indicated. (*B*) Enlarged views of the potential cyt. c_z docking site. The binding site enclosed by the dashed box is enlarged in the *Right* panel. The distances of the heme iron to the Mg^{2+} ions of P_{840} are 23.3 and 21.9 Å (red dotted lines), respectively. The propionate group of ring C is at a distance of 2.4 Å from $W601^{PscA}$. (*C*) Electrostatic surface representation of the FMO-GsbRC complex showing the potential docking site for ferredoxin. A homology model of the ferredoxin from *C. tepidum* (Uniprot: Q8KCZ6) was built using Alphafold. Several positively charged residues are in the proximity of the potential docking site (enlarged view in the *Right*).

the role of the PscD in the ET to ferrodoxin appears to be additive and not too serious, since a GsbRC mutant lacking PscD exhibited only minor effects on the ferredoxin-mediated photosynthetic ET (29).

As mentioned above, the existence of a supercomplex consisting of two GsbRCs and four FMO trimers has previously been suggested (15). We could construct a structural model for the FMO-GsbRC supercomplex, in which the two FMO-GsbRC complexes face each other across the interaction interface with their ferredoxin binding sites facing outwards (*SI Appendix*, Fig. S12 and Movie S3). This model suggests that both FMO-GsbRC complexes are loosely associated with each other only through interactions between the soluble FMO proteins. Future studies would be necessary to investigate the biological significance and the functional relevance of this photosynthetic supercomplex.

Downloaded from https://www.pnas.org by MPDL BIOPHYSIK on February 16, 2023 from IP address 194.95.30.10.

The cryo-EM structure of the whole FMO-GsbRC complex reveals many characteristic features of the homodimeric type I RC from GSB with an overall asymmetrical architecture, fewer associated pigments and a distinctive pigment arrangement that establishes the energy transfer pathways. These results provide a basis for a more comprehensive examination of the energy and electron transfer functions of this photosynthetic complex through both experimental and theoretical approaches.

Materials and Methods

Purification of the Whole RC. *C. tepidum* TLS (formerly known as *Chlorobium tepidum*), obtained from Prof. H. Sakurai (Waseda University, Tokyo), was grown in Pf-7 medium (9). Cultures (10 L) were incubated at 47 °C under continuous illumination from 2 W illuminating tubes at 20 μE m^{-2} s^{-1}. Cells were harvested after 2 d by centrifugation at 8,000 × *g* for 15 min. The RC was purified by a method reported previously with the following modifications (14). Cells were resuspended in 20 mM HEPES, pH 8, 20 μM flavin mononucleotide (FMN) and were disrupted three times by passing through a French pressure cell at 18,000 psi. The crude cell lysate was centrifuged at 20,000 × *g* for 20 min and the membranes were sedimented at 120,000 × *g* for 1 h. Crude membranes were resuspended in wash buffer (20 mM HEPES, pH 8, 150 mM NaCl, 20 μM FMN and 1 mM EDTA), and sedimented as before. The washed membranes were resuspended again in wash buffer to an optical density at 750 nm of 200 or greater and stored at −20 °C. For solubilization, the optical density at 750 nm of the membrane solution was adjusted to 150, and 2% (w/v) DDM was added. The mixture was stirred in the dark at 4 °C for 90 min. The insoluble membrane fraction was removed by centrifugation at 211,000 × *g* for 1 h. The supernatant containing solubilized membrane proteins was fractionated by a five-step sucrose gradient (10%, 20%, 30%, 40%, and 50% [w/v] sucrose) in 20 mM HEPES, pH 8, 150 mM NaCl, 1 mM EDTA and 0.02% DDM. After 17 h centrifugation at 250,000 × *g*, the green band was collected and loaded onto an DEAE ion-exchange column pre-equilibrated with 20 mM HEPES, pH 8, 150 mM NaCl, 1 mM EDTA and 0.01% (w/v) LMNG. Green fractions of the flow-through, containing the RC, were collected and concentrated using Amicon Ultra-15 concentrators (100K MWCO). To isolate the whole RC complex, concentrated proteins were further purified using a combination of GraDeR (17) and GraFix (18). A continuous linear gradient was prepared by mixing the light solution containing 20 mM HEPES, pH 8, 100 mM NaCl, 1 mM EDTA, 10% (w/v) sucrose and 0.01% (w/v) LMNG and the heavy solution containing 20 mM HEPES, pH 8, 100 mM NaCl, 1 mM EDTA, 25% sucrose (w/v) and 0.15% glutaraldehyde (v/v). Centrifugation was performed at 250,000 × *g* and 4 °C for 17 h. After centrifugation, four different colored bands were observed (RC1 to RC4, *SI Appendix*, Fig. S1). Peak fractions containing the whole RC complex (RC4, *SI Appendix*, Fig. S1) were pooled and the crosslinking reaction was quenched with 100 mM Tris (pH 8.0). Purified samples were dialyzed against buffer (20 mM HEPES, pH 8, 100 mM NaCl, 1 mM EDTA) overnight at 4 °C using D-tube dialyzer Maxi (MWCO 12-14 kDa, Millipore), and were concentrated using Amicon Ultra-15 concentrators (100K MWCO).

Cryo-EM Sample Preparation and Data Acquisition. Prior to cryo-EM data collection, purified RC samples were negatively stained with 2% (w/v) uranyl formate and analyzed by negative-stain electron microscopy with a Rio16 CMOS camera (Gatan) on a Tecnai Spirit (FEI Company) transmission electron microscope (TEM) operated at 120 kV. Automated data collection was carried out using Leginon (47). Image processing was carried out using cisTEM (48).

For cryo-EM sample preparation, purified proteins were diluted to an absorbance of 0.01 at 602 nm. An aliquot of 3 μL of purified protein was applied onto freshly glow-discharged Quantifoil carbon-coated grids (R1.2/1.3 + 2 nm carbon layer, Cu, 200 mesh). Samples were vitrified using a Vitrobot Mk IV (Thermo Scientific) by blotting at nominal blot force −2 for 4 s at 4 °C and 100% relative humidity and plunging grids into liquid ethane.

High-resolution cryo-EM imaging was performed using a Titan Krios G3i TEM (Thermo Scientific) operated at 300 kV and equipped with a BioQuantum-K3 imaging filter (Gatan). Cryo-EM data were collected in electron counting super-resolution mode at a nominal magnification of 105,000×. To overcome the problem of preferred specimen orientation, data were collected at 0°, 20°, and 25° sample tilts. A total of 19,826 movies were acquired with a total dose of ~45 e^{-}/ $Å^2$ (50 frames) using EPU software (Thermo Scientific). A defocus range from −1.2 to −2.5 μm was applied for data collection, and cryoSPARC live was employed for constantly monitoring the quality of the incoming movies and for the on-the-fly data processing.

Cryo-EM Image Processing. A detailed data processing workflow is summarized in *SI Appendix*, Fig. S2. For the whole RC complex, image processing was performed with cryoSPARC (49) and Relion 3.0 (50) using dose-weighted micrographs. For cryoSPARC, all movies were motion-corrected and contrast transfer function (CTF)-estimated with cryoSPARC's own implementation. A total of 4,791.019 raw particles were auto-picked without reference using blob picker and subjected to reference-free 2-dimensional (2D) classification. After two rounds of 2D classification, 653,665 particles were selected based on protein complex integrity and were used for Ab-Initio reconstruction with two classes. A subset of 481,095 particles from the class with two bound FMO trimers was selected and subjected to a second round of ab initio reconstruction. A total of 406,190 particles were selected and refined using non-uniform (NU) refinement with imposition of C1 symmetry, yielding a reconstruction with 2.57 Å resolution. After local- and global-CTF refinement, the resulting model was further improved in a second NU-refinement step using C1 symmetry, yielding a map with a resolution of 2.50 Å according to the 0.143 cutoff criterion (51). This final map was used to build the atomic model for the whole RC complex.

For data processing using Relion, all movies were subjected to beam-induced motion correction using MotionCor2 (52). Afterward, motion-corrected micrographs were CTF-estimated using CTFFIND4 (53). The coordinates of 481,095 particles, which were mentioned above, were converted to the Relion star file using "csparc2star.py" from UCSF pyem (54). The particles were extracted and subjected to the 3D classification. After 3D refinement, CTF refinement, and Bayesian polishing, selection of 406,007 particles resulted in a reconstruction with an overall resolution of 2.58 Å.

Model Building and Refinement. Before the cryo-EM structure of the FMO-GsbRC subcomplex was available (16), we had independently built a structural model for GsbRC based on our cryo-EM data. Therefore, the published structure (PDB: 6M32) was not used as a template for modeling in this study. For the FMO trimer, the model was built by fitting the crystal structure of the FMO protein (PDB: 3ENI) from *C. tepidum* into the obtained density map (33). For PscA subunit, a homology model was first generated by SWISS-MODEL (55) based on the crystal structure of type I RC from *Heliobacterium modesticaldum* (24). This homology model was fitted into the density and further built and modified using Coot (56). For PscB, PscC, and PscD, partial structural information was obtained using a combination of SWISS-MODEL (55), Jpred (57), TMHMM (58), and ARP/wARP 8.0 (59). The model of PscB was built initially by tracing the [4Fe–4S] clusters and their surrounding residues. For PscC and PscD, poly-alanine alpha helices were manually placed into the respective density and subsequently corrected, extended using Coot. Chlorophyll molecules were obtained from the Coot monomer library (BCL for BChl *a* and CLA for chlorophyll *a*, respectively). The model of the glycosylated chlorobactene (F39) was adopted from the previously reported structure of FMO-GsbRC subcomplex (16). The model of the MGDG was built using Coot Ligand Builder. Restraints for all ligands were generated by eLBOW in Phenix (60). The initial model was refined using phenix.real_space_refine (61) and further improved by iterative rounds of the manual model building using Coot. The final model was validated using MolProbity (62) and PHENIX (63, 64). Statistics of the map reconstruction and model refinement are shown in *SI Appendix*, Table S1. Model representations in the figures and movies were prepared using UCSF Chimera (65) and UCSF ChimeraX (66).

Miscellaneous Methods. Sodium dodecyl sulfate–polyacrylamide gel electrophoresis analysis was performed using 4 to 12% Bis-Tris NuPAGE gels (Invitrogen) followed by Coomassie blue staining. BN-PAGE was performed using Novex 4 to 16% Bis-Tris gels (Invitrogen) according to the manufacturer's instructions. UV-visible (UV–VIS) spectra of the purified RC samples were recorded on a Lambda 35 UV-VIS spectrometer (PerkinElmer). The protein disordered region analysis was were conducted using PrDOS (67). The cyt. *c*-binding site of the GsbRC was analyzed by protein-protein docking using HDOCK (68).

Data, Materials, and Software Availability. The electron density map and model of the photosynthetic complex have been deposited in the Electron Microscopy Data Bank (https://www.ebi.ac.uk/emdb/) under accession number

Downloaded from https://www.pnas.org by MPDL BIOPHYSIK on February 16, 2023 from IP address 194.95.30.10.

EMD-14528 (69) and in the Protein Data Bank (https://www.rcsb.org) under accession number 7Z6Q (70), respectively.

ACKNOWLEDGMENTS. We would like to thank Simone Prinz, Dr. Susann Kaltwasser and Mark Linder at the Central Electron Microscopy Facility at the Max Planck Institute of Biophysics for their support and assistance with microscopy data collection. We thank Katerina Aktoudianaki and Dimitris Dedoglou for the cultivation of *C. tepidum*. Funding: This work was supported by the Max Planck Society, the University of Crete and the Greek Ministry of Education.

Author affiliations: [a]Department of Molecular Membrane Biology, Max Planck Institute of Biophysics, Frankfurt am Main D-60438, Germany; [b]Department of Chemistry, University of Crete, Voutes Heraklion GR-70013, Greece; and [c]Central Electron Microscopy Facility, Max Planck Institute of Biophysics, Frankfurt am Main D-60438, Germany

1. M. F. Hohmann-Marriott, R. E. Blankenship, Evolution of photosynthesis. *Annu. Rev. Plant Biol.* **62**, 515–548 (2011).
2. R. G. Saer, R. E. Blankenship, Light harvesting in phototrophic bacteria: Structure and function. *Biochem. J.* **474**, 2107–2131 (2017).
3. T. Cardona, Thinking twice about the evolution of photosynthesis. *Open Biol.* **9**, 180246 (2019).
4. R. E. Blankenship, Origin and early evolution of photosynthesis. *Photosyn. Res.* **33**, 91–111 (1992).
5. C. J. Gisriel, C. Azai, T. Cardona, Recent advances in the structural diversity of reaction centers. *Photosyn. Res.* **149**, 329–343 (2021).
6. G. S. Orf, R. E. Blankenship, Chlorosome antenna complexes from green photosynthetic bacteria. *Photosyn. Res.* **116**, 315–331 (2013).
7. J. T. Nielsen *et al.*, In situ high-resolution structure of the baseplate antenna complex in Chlorobaculum tepidum. *Nat. Commun.* **7**, 12454 (2016).
8. J. M. Tsuji *et al.*, Anoxygenic phototrophic Chloroflexota member uses a Type I reaction center. bioRxiv [Preprint] (2020). https://doi.org/10.1101/2020.07.07.190934 (Accessed 7 July 2020).
9. T. M. Wahlund, C. R. Woese, R. W. Castenholz, M. T. Madigan, A thermophilic green sulfur bacterium from New Zealand hot springs. *Chlorobium tepidum sp. nov. Arch. Microbiol.* **156**, 81–90 (1991).
10. G. Hauska, T. Schoedl, H. Remigy, G. Tsiotis, The reaction center of green sulfur bacteria. *Biochim. Biophys. Acta Bioenerg.* **1507**, 260–277 (2001).
11. H. Oh-oka, M. Iwaki, S. Itoh, Membrane-bound cytochrome cz couples quinol oxidoreductase to the P840 reaction center complex in isolated membranes of the green sulfur bacterium Chlorobium tepidum. *Biochemistry* **37**, 12293–12300 (1998).
12. M. Higuchi *et al.*, Overexpression, characterization, and crystallization of the functional domain of cytochrome c(z) from Chlorobium tepidum. *Photosyn. Res.* **102**, 77–84 (2009).
13. G. He, H. Zhang, J. D. King, R. E. Blankenship, Structural analysis of the homodimeric reaction center complex from the photosynthetic green sulfur bacterium Chlorobaculum tepidum. *Biochemistry* **53**, 4924–4930 (2014).
14. H. W. Rémigy *et al.*, The reaction center complex from the green sulfur bacterium Chlorobium tepidum: A structural analysis by scanning transmission electron microscopy. *J. Mol. Biol.* **290**, 851–858 (1999).
15. D. Bína, Z. Gardian, F. Vácha, R. Litvín, Native FMO-reaction center supercomplex in green sulfur bacteria: An electron microscopy study. *Photosyn. Res.* **128**, 93–102 (2016).
16. J.-H. Chen *et al.*, Architecture of the photosynthetic complex from a green sulfur bacterium. *Science* **370**, eabb6350 (2020).
17. F. Hauer *et al.*, GraDeR: Membrane protein complex preparation for single-particle cryo-EM. *Structure* **23**, 1769–1775 (2015).
18. H. Stark, GraFix: Stabilization of fragile macromolecular complexes for single particle Cryo-EM. Cryo-EM part a sample preparation and data collection. *Elsevier* **481**, 109–126 (2010).
19. S. Takaichi *et al.*, New carotenoids from the thermophilic green sulfur bacterium Chlorobium tepidum: 1′,2′-dihydro-gamma-carotene, 1′,2′-dihydrochlorobactene, and OH-chlorobactene glucoside ester, and the carotenoid composition of different strains. *Arch. Microbiol.* **168**, 270–276 (1997).
20. S. Takaichi, H. Oh-oka, Pigment composition in the reaction center complex from the thermophilic green sulfur bacterium, Chlorobium tepidum: Carotenoid glucoside esters, menaquinone and chlorophylls. *Plant Cell Physiol.* **40**, 691–694 (1999).
21. P. G. Sørensen, R. P. Cox, M. Miller, Chlorosome lipids from Chlorobium tepidum: Characterization and quantification of polar lipids and wax esters. *Photosyn Res.* **95**, 191–196 (2008).
22. Y. Saga, N. Yoshida, S. Yamada, T. Mizoguchi, H. Tamiaki, Biosynthesis of unnatural glycolipids possessing diyne moiety in the acyl chain in the green sulfur photosynthetic bacterium Chlorobaculum tepidum grown by supplementation of 10,12-heptadecadiynic acid. *Biochem. Biophys. Rep.* **9**, 42–46 (2017).
23. G. Tsiotis, C. Hager-Braun, B. Wolpensinger, A. Engel, G. Hauska, Structural analysis of the photosynthetic reaction center from the green sulfur bacterium Chlorobium tepidum. *Biochim. Biophys. Acta Bioenerget.* **1322**, 163–172 (1997).
24. C. Gisriel *et al.*, Structure of a symmetric photosynthetic reaction center-photosystem. *Science* **357**, 1021–1025 (2017).
25. Y. Hirano *et al.*, Crystal structure of the electron carrier domain of the reaction center cytochrome c(z) subunit from green photosynthetic bacterium Chlorobium tepidum. *J. Mol. Biol.* **397**, 1175–1187 (2010).
26. H. Oh-oka, M. Iwaki, S. Itoh, Viscosity dependence of the electron transfer rate from bound cytochrome c to P840 in the photosynthetic reaction center of the green sulfur bacterium Chlorobium tepidum. *Biochemistry* **36**, 9267–9272 (1997).
27. P. Jordan *et al.*, Three-dimensional structure of cyanobacterial photosystem I at 2.5 A resolution. *Nature* **411**, 909–917 (2001).
28. M. Hippler, F. Drepper, W. Haehnel, J. D. Rochaix, The N-terminal domain of PsaF: Precise recognition site for binding and fast electron transfer from cytochrome c6 and plastocyanin to photosystem I of Chlamydomonas reinhardtii. *Proc. Natl. Acad. Sci. U.S.A.* **95**, 7339–7344 (1998).
29. Y. Tsukatani, R. Miyamoto, S. Itoh, H. Oh-Oka, Function of a PscD subunit in a homodimeric reaction center complex of the photosynthetic green sulfur bacterium Chlorobium tepidum studied by insertional gene inactivation. Regulation of energy transfer and ferredoxin-mediated NADP+ reduction on the cytoplasmic side. *J. Biol. Chem.* **279**, 51122–51130 (2004).
30. C. Hager-Braun *et al.*, Stable photobleaching of P840 in Chlorobium reaction center preparations: Presence of the 42-kDa bacteriochlorophyll a protein and a 17-kDa polypeptide. *Biochemistry* **34**, 9617–9624 (1995).
31. M. A. Lomize, I. D. Pogozheva, H. Joo, H. I. Mosberg, A. L. Lomize, OPM database and PPM web server: Resources for positioning of proteins in membranes. *Nucleic. Acids. Res.* **40**, D370–D376 (2012).
32. A. Ben-Shem, F. Frolow, N. Nelson, Evolution of photosystem I–From symmetry through pseudo-symmetry to asymmetry. *FEBS Lett.* **564**, 274–280 (2004).
33. D. E. Tronrud, J. Wen, L. Gay, R. E. Blankenship, The structural basis for the difference in absorbance spectra for the FMO antenna protein from various green sulfur bacteria. *Photosyn. Res.* **100**, 79–87 (2009).
34. J. Wen, H. Zhang, M. L. Gross, R. E. Blankenship, Membrane orientation of the FMO antenna protein from Chlorobaculum tepidum as determined by mass spectrometry-based footprinting. *Proc. Natl. Acad. Sci. U.S.A.* **106**, 6134–6139 (2009).
35. M. Schmidt am Busch, F. Müh, M. El-Amine Madjet, T. Renger, The eighth bacteriochlorophyll completes the excitation energy funnel in the FMO protein. *J. Phys. Chem. Lett.* **2**, 93–8 (2011).
36. J. Cao *et al.*, Quantum biology revisited. *Sci. Adv.* **6**, eaaz4888 (2020).
37. C. Kreisbeck, T. Kramer, M. Rodríguez, B. Hein, High-performance solution of hierarchical equations of motion for studying energy transfer in light-harvesting complexes. *J. Chem. Theory. Comput.* **7**, 2166–2174 (2011).
38. J. Moix, J. Wu, P. Huo, D. Coker, J. Cao, Efficient energy transfer in light-harvesting systems, III: The influence of the eighth bacteriochlorophyll on the dynamics and efficiency in FMO. *J. Phys. Chem. Lett.* **2**, 3045–3052 (2011).
39. G. He, D. M. Niedzwiedzki, G. S. Orf, H. Zhang, R. E. Blankenship, Dynamics of energy and electron transfer in the FMO-reaction center core complex from the phototrophic green sulfur bacterium chlorobaculum tepidum. *J. Phys. Chem. B.* **119**, 8321–8329 (2015).
40. J. Dostál, J. Pšenčík, D. Zigmantas, In situ mapping of the energy flow through the entire photosynthetic apparatus. *Nat. Chem.* **8**, 705–710 (2016).
41. I. Caspy, N. Nelson, Structure of the plant photosystem I. *Biochem. Soc. Trans.* **46**, 285–94 (2018).
42. Y. Umena, K. Kawakami, J.-R. Shen, N. Kamiya, Crystal structure of oxygen-evolving photosystem II at a resolution of 1.9 Å. *Nature* **473**, 55–60 (2011).
43. Y. Tsukatani, C. Azai, T. Kondo, S. Itoh, H. Oh-Oka, Parallel electron donation pathways to cytochrome c(z) in the type I homodimeric photosynthetic reaction center complex of Chlorobium tepidum. *Biochim. Biophys. Acta.* **1777**, 1211–1217 (2008).
44. A. Kölsch *et al.*, Insights into the binding behavior of native and non-native cytochromes to photosystem I from Thermosynechococcus elongatus. *J. Biol. Chem.* **293**, 9090–9100 (2018).
45. H. L. Axelrod *et al.*, X-ray structure determination of the cytochrome c2: Reaction center electron transfer complex from Rhodobacter sphaeroides. *J. Mol. Biol.* **319**, 501–515 (2002).
46. H. Kubota-Kawai *et al.*, X-ray structure of an asymmetrical trimeric ferredoxin-photosystem I complex. *Nat. Plants.* **4**, 218–224 (2018).
47. C. Suloway *et al.*, Automated molecular microscopy: The new Leginon system. *J. Struct. Biol.* **151**, 41–60 (2005).
48. T. Grant, A. Rohou, N. Grigorieff, cisTEM, user-friendly software for single-particle image processing. *Elife* **7**, e35383 (2018).
49. A. Punjani, J. L. Rubinstein, D. J. Fleet, M. A. Brubaker, cryoSPARC: Algorithms for rapid unsupervised cryo-EM structure determination. *Nat Methods* **14**, 290–296 (2017).
50. S. H. W. Scheres, RELION: Implementation of a Bayesian approach to cryo-EM structure determination. *J. Struct. Biol.* **180**, 519–530 (2012).
51. P. B. Rosenthal, R. Henderson, Optimal determination of particle orientation, absolute hand, and contrast loss in single-particle electron cryomicroscopy. *J. Mol. Biol.* **333**, 721–745 (2003).
52. S. Q. Zheng *et al.*, MotionCor2: Anisotropic correction of beam-induced motion for improved cryo-electron microscopy. *Nat. Methods* **14**, 331–332 (2017).
53. A. Rohou, N. Grigorieff, CTFFIND4: Fast and accurate defocus estimation from electron micrographs. *J. Struct. Biol.* **192**, 216–221 (2015).
54. D. Asarnow, E. Palovcak, Y. Cheng, asarnow/pyem: UCSF pyem v0.5. Zenodo (2019).
55. T. Schwede, J. Kopp, N. Guex, M. C. Peitsch, SWISS-MODEL: An automated protein homology-modeling server. *Nucleic. Acids Res.* **31**, 3381–3385 (2003).
56. P. Emsley, K. Cowtan, Coot: Model-building tools for molecular graphics. *Acta Crystallogr. Sect. D. Biol. Crystallogr.* **60**, 2126–2132 (2004).
57. C. Cole, J. D. Barber, G. J. Barton, The Jpred 3 secondary structure prediction server. *Nucleic. Acids Res.* **36**, W197–W201 (2008).
58. A. Krogh, B. Larsson, G. von Heijne, E. L. L. Sonnhammer, Predicting transmembrane protein topology with a hidden Markov model: Application to complete genomes. *J. Mol. Biol.* **305**, 567–580 (2001).
59. G. Chojnowski, P. Heuser, J. Pereira, V. Lamzin, Building atomic models into electron microscopy maps with ARP/wARP version 8.0. *Acta. Crystallogr. A. Found. Adv.* **74**, e151–e151 (2018).
60. N. W. Moriarty, R. W. Grosse-Kunstleve, P. D. Adams, Electronic Ligand Builder and optimization workbench (eLBOW): A tool for ligand coordinate and restraint generation. *Acta. Crystallogr. Sect. D. Biol. Crystallogr.* **65**, 1074–1080 (2009).
61. P. V. Afonine *et al.*, New tools for the analysis and validation of cryo-EM maps and atomic models. *Acta. Crystallogr. D. Struct. Biol.* **74**, 814–840 (2018).
62. C. J. Williams *et al.*, MolProbity: More and better reference data for improved all-atom structure validation. *Protein. Sci.* **27**, 293–315 (2018).
63. D. Liebschner *et al.*, Macromolecular structure determination using X-rays, neutrons and electrons: Recent developments in Phenix. *Acta. Crystallogr. D. Struct. Biol.* **75**, 861–877 (2019).
64. P. D. Adams *et al.*, PHENIX: Building new software for automated crystallographic structure determination. *Acta. Crystallogr. Sect. D. Biol. Crystallogr.* **58**, 1948–1954 (2002).

Downloaded from https://www.pnas.org by MPDL BIOPHYSIK on February 16, 2023 from IP address 194.95.30.10.

65. E. F. Pettersen *et al.*, UCSF Chimera–A visualization system for exploratory research and analysis. *J. Comput. Chem.* **25**, 1605–1602 (2004).
66. T. D. Goddard *et al.*, UCSF ChimeraX: Meeting modern challenges in visualization and analysis. *Protein. Sci.* **27**, 14–25 (2018).
67. T. Ishida, K. Kinoshita, PrDOS: Prediction of disordered protein regions from amino acid sequence. *Nucleic. Acids. Res.* **35**, W460–W464 (2007).
68. Y. Yan, D. Zhang, P. Zhou, B. Li, S.-Y. Huang, HDOCK: A web server for protein-protein and protein-DNA/RNA docking based on a hybrid strategy. *Nucleic. Acids. Res.* **45**, W365–W373 (2017).
69. H. Xie, G. Tsiotis, Cryo-EM structure of the whole photosynthetic complex from the green sulfur bacteria. *Electron Microscopy Data Bank*. https://www.ebi.ac.uk/emdb/EMD-14528. Deposited 14 March 2022.
70. H. Xie, G. Tsiotis, Cryo-EM structure of the whole photosynthetic complex from the green sulfur bacteria. *Protein Data Bank*. https://www.rcsb.org/structure/7Z6Q. Deposited 14 March 2022.

Downloaded from https://www.pnas.org by MPDL BIOPHYSIK on February 16, 2023 from IP address 194.95.30.10.